Journal of
Sensor and Actuator Networks

MDPI

Article

Multi-Domain Feature Engineering for Noise-Tolerant Fault Classification in Analog Filter Circuits

Archana Dhamotharan [1,*], Balakumar Muniandi [2,*], Vennila Anandaraj Umapathy [1,†], Neya Subramanian [1,†] and Sowmiya Balamurugan [1,†]

[1] Electronics and Communication Engineering, PSG Institute of Technology and Applied Research, Coimbatore 641062, India; vennilaanandraj27@gmail.com (V.A.U.); neyakrr@gmail.com (N.S.); bsowmiya4282@gmail.com (S.B.)
[2] Electrical and Computer Engineering, University of Idaho, Moscow, ID 83844, USA
* Correspondence: ece04kpr@gmail.com (A.D.); bmuniandi@uidaho.edu (B.M.)
† These authors contributed equally to this work.

Abstract

This paper proposes a method of fault detection in analog circuits which involves various steps, including selection of benchmark circuits, dataset preparation, signal decomposition, model training, and performance analysis. The main aim of this work is to provide solid performance even in noisy environments. Monte Carlo analysis is used to generate a synthetic dataset with 200 runs per fault class by introducing component tolerances and realistic faults. A multi-stage pipeline is proposed; it begins with resampling the signals and normalizing them, and then noise is added at different levels: 5 dB, 10 dB and 20 dB. Feature fusion is performed by combining time-, frequency-, and statistical-domain features. Statistical-domain features are extracted by applying Variational Mode Decomposition (VMD) to split them into four IMF levels, followed by the application of Continuous Wavelet Transform (CWT) for time–frequency-domain analysis. Support Vector Machine (SVM), Random Forest, and Gradient Boosting are used as base-level classification models. A stacking ensemble model is developed which uses Random Forest, Gradient Boosting, and Extra Trees as base learners and Logistic Regression as the meta-learner.

Keywords: analog filter circuits; fault diagnosis; Monte Carlo simulation; variational mode decomposition; continuous wavelet transform; additive white Gaussian noise; stacking ensemble learning; noise analysis

Check for updates

Academic Editors: Mingjian Zuo, Xiaoguang Zhang, Xiuxiu Ren and Yiyang Liu

Received: 19 April 2026
Revised: 24 June 2026
Accepted: 30 June 2026
Published: 13 July 2026

Copyright: © 2026 by the authors. Licensee MDPI, Basel, Switzerland. This article is an open access article distributed under the terms and conditions of the Creative Commons Attribution (CC BY) license.

1. Introduction

Analog circuits have many applications in daily life, including signal processing systems, biomedical sensors, power electronics, wireless communications, and audio processing. Analog circuits experience variations due to tolerance, which are the result of factors including aging, manufacturing, environment, and operational usage. Parametric (soft) faults can be very difficult to diagnose as opposed to hard faults because the soft faults do not cause an immediate failure and will allow the circuit to continue to operate but will degrade the quality of the circuit's performance.

As the faults progress, it becomes increasingly more difficult to diagnose the faults. Manual testing was the first approach to diagnose analog circuits. This method included simple DC limits and function signature. However, these methods were inadequate for detecting subtle changes in the circuit parameters. In order to improve the performance of

diagnostic techniques, simulation-based testing was implemented. Two types of simulation-based testing include Simulation Before Test (SBT) and Simulation After Test (SAT) [1]. SBT includes simulating both faulty and fault-free conditions and comparing the output signatures. This method improved the accuracy of diagnostics; however, it had limited usability and was sensitive to noise. SAT also provides a more flexible framework and allows for adjusting the values of components based on their specified tolerance and allows the user to adjust the circuit model to better fit the actual measured data. The disadvantage of SAT is its increased computational complexity.

The implementation of machine learning in the area of fault detection has dramatically changed the diagnostic process for analog circuits. Analog fault diagnosis is now viewed as a multi-class pattern recognition problem [2]. Dieste-Velasco proposed a voltage-measurement-based feature extraction methodology for seven classifiers, in which ANN and SVM achieve higher performance for soft fault classification in a basic Sallen–Key bandpass filter circuit, followed by KNN and DAC, while Random Forest, despite having a high training accuracy, dropped significantly during testing indicating overfitting, and CDT and Naïve Bayes proved to be the least effective classifiers. It did show ambiguity for some fault classes which are seen across all models [3]. He also proposed a hybrid PSO–machine learning approach for identifying simultaneous soft faults across 83 fault classes in a Sallen–Key bandpass filter, where two hybrid models were evaluated—RF-PSO and PSO-ANN—with RF-PSO achieving superior training performance across all metrics (accuracy: 98.24%, precision: 98.28%, recall: 98.24%, F1-score: 98.24%, MCC: 98.22%) but suffering a significant drop on test data (accuracy: 86.43%, F1-score: 85.90%) indicating overfitting, while PSO-ANN demonstrated more balanced generalization with training metrics of 94.26% accuracy and MCC of 94.19%, maintaining stable test performance (accuracy: 93.01%, MCC: 92.93%), correctly classifying 39 out of 83 classes, and critically outperforming RF-PSO in detecting the nominal class—a decisive criterion since misclassifying faulty circuits as nominal poses the greatest operational risk [4]. Aminian contributed to the area of analog fault detection using the wavelet transform as a means to extract features with an artificial neural network (ANN) architecture [5]. His work on the Sallen–Key bandpass filter benchmark resulted in a diagnostic accuracy of 94.11%. He stated that using time–frequency representations resulted in better diagnostic accuracy than simply using either time- or frequency-domain statistics.

Wavelet-based methods can be difficult as they depend on picking the right basis function, like Daubechies, Morlet or Meyer. If a wrong basis function is chosen, it degrades the features extracted. To fix this issue, researchers lately have opted for data-driven adaptive decomposition instead. It seems more flexible this way. For instance, Zhao and others tried Ensemble Empirical Mode Decomposition (EEMD) on the Sallen–Key filter [6]. They broke the signals down into four intrinsic mode functions (IMFs). Then they used the Maximum Information Coefficient for cutting down dimensions, and a Particle Swarm Optimization SVM classifier on top [7]. That got them a diagnostic accuracy of 99.88 per cent, which is impressive.

Further improvements were made by Lu et al. [8], who used Variational Mode Decomposition (VMD) to solve the mode-mixing issues that were present in EMD. By computing Mathematical Morphology Fractal Dimensions (MMFDs) for each IMF, they captured fault-induced changes in geometric complexity. They achieved 96.3% accuracy across 15 fault classes. Ma et al. extended this VMD-based approach into a multi-feature fusion framework by integrating Composite Multi-Scale Entropy (CMSE), time-domain statistics, and frequency-domain parameters [9]. Their use of Deep Generalized Canonical Correlation Analysis (DGCCA) to fuse these features resulted in a 99.20% accuracy rate, which is more than traditional ELM and DCNN benchmarks.

Deep learning architectures introduce automatic feature learning from raw waveforms. Yang et al. utilized 1D-CNNs to bypass manual feature engineering, while Yuan et al. [10] developed dual-stream CNNs introducing Continuous Wavelet Transform (CWT) scalograms with hybrid CNN-LSTM frameworks, improving accuracies to 98.96% for second-order filters.

Despite these advancements, there are some limitations that still persist. Firstly, in most of the existing works, the circuits are tested under ideal or near-ideal conditions (SNR > 20 dB) whereas most circuits operate under noisy conditions with SNR levels of 5 to 20 dB. Gao et al. [11] have shown that accuracy degrades sharply below 15 dB and there is a lack of research to characterize this degradation at the individual IMF level. Secondly, most of the models perform analysis at a single domain, whereas most of the characteristics are observed in a multi-domain feature set.

The specific contributions of this work are as follows: (1) simultaneous validation on two structurally distinct benchmark topologies, namely the Sallen–Key bandpass filter and the four-op-amp biquad high-pass filter; (2) combining time-domain, frequency-domain, and intrinsic mode function (IMF) features into a single feature vector; (3) analyzing how noise affects each IMF level using mean squared error (MSE) at three signal-to-noise ratio (SNR) levels (5, 10, and 20 dB); and (4) a topological ambiguity analysis that attributes residual misclassification to circuit observability constraints rather than classifier limitations. This paper addresses these gaps by proposing a noise-aware, multi-feature stacking ensemble framework.

2. Methodology

The proposed fault diagnosis framework is demonstrated as a multi-stage pipeline in Figure 1, illustrating the complete process from circuit selection and simulation through feature extraction, model training, and performance evaluation.

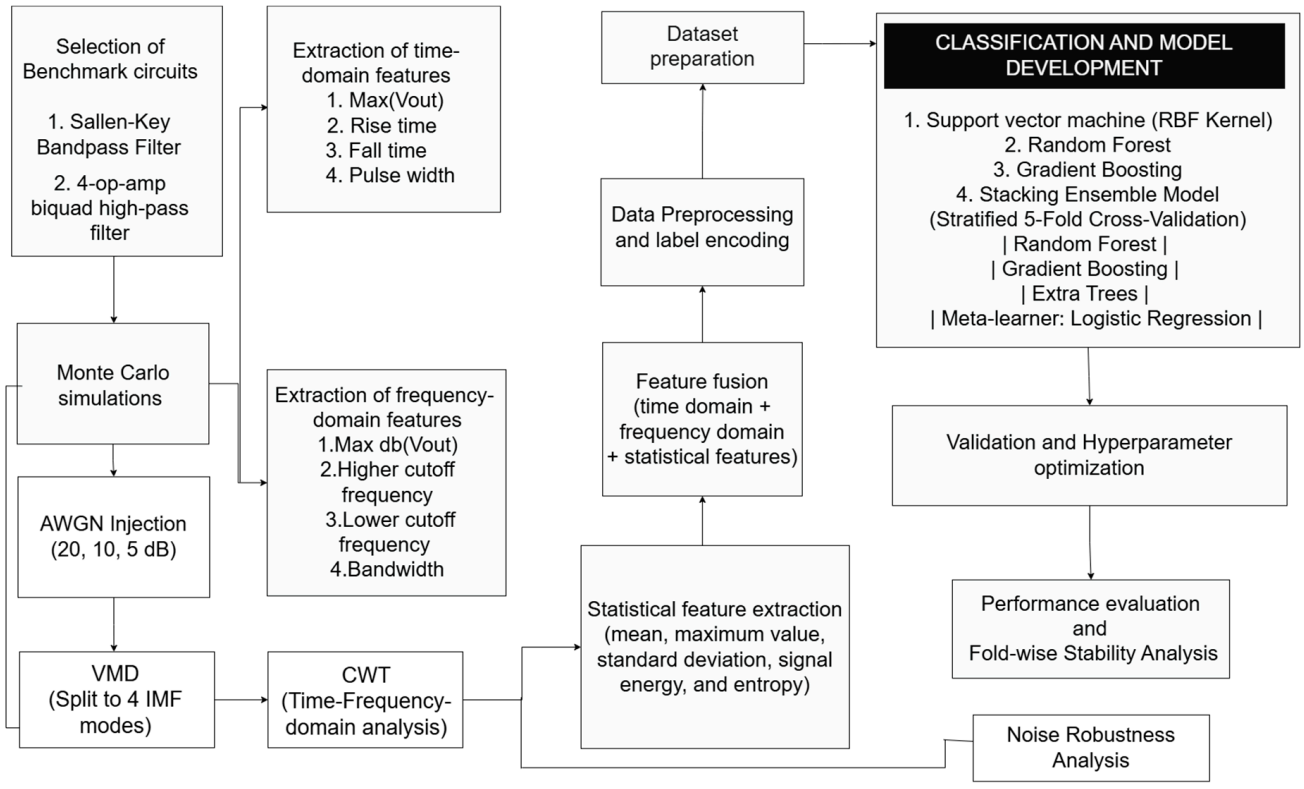


Figure 1. Outline of the proposed fault diagnosis framework.

2.1. Circuit Topologies and Fault Modeling

To thoroughly assess the proposed methodology, two benchmark analog filter circuits with different topology and complexity levels are selected. These circuits are used as standard building blocks in signal processing chains where reliability is important.

2.1.1. Benchmark Architectures

1. Second-Order Sallen–Key Bandpass Filter

The Sallen–Key bandpass filter is used as the first benchmark in this study. As shown in the simulation schematic (Figure 2), the circuit uses a single-supply configuration (5 V) with a 2.5 V DC bias to establish a virtual ground. The nominal passive component values are $C_1 = C_2 = 10$ nF, $C_3 = 2.2$ nF, and $C_4 = 1.1$ nF, with a resistive network of $R_1 = 23$ kΩ, $R_2 = 11$ kΩ, and $R_3 = R_4 = 10$ kΩ.

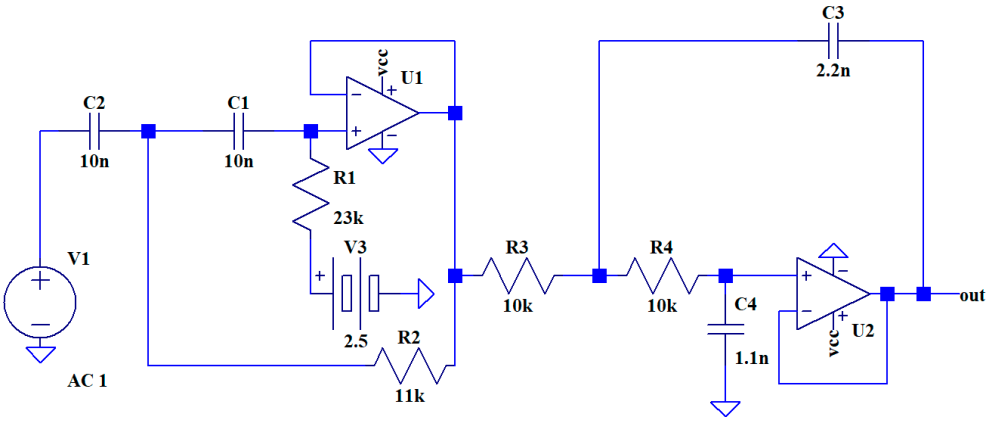


Figure 2. Schematic diagram of the second-order Sallen–Key bandpass filter.

The ideal transfer function $H(s)$ for this topology, which serves as the mathematical baseline for feature extraction, is defined as follows:

$$H(s) = \frac{K \cdot (\frac{s}{R_1 C_1})}{s^2 + s(\frac{1}{R_1 C_1} + \frac{1}{R_2 C_2} + \frac{(1-K)}{R_2 C_1}) + \frac{1}{R_1 R_2 C_1 C_2}}, \quad (1)$$

where K represents the passband gain and s represents the laplace variable which is used to analyze circuit behavior in the frequency domain. Any parametric drift in these components directly shifts the poles of the system, altering the transient response analyzed in later stages.

2. Fourth-Order Four-Op-Amp Biquad High-Pass Filter

The fourth-order high-pass filter realized with a four-op-amp biquadratic topology serves as the second benchmark circuit [10] (Figure 3) which is more complex. This architecture is chosen for its high sensitivity to component variations and its ability to provide independent tuning of the quality factor (Q) and natural frequency (ω_0). The circuit operates on a dual symmetrical supply of ±12 V. The critical frequency-determining components are $C_1 = C_2 = 5$ nF, $R_1 = R_3 = 6.2$ kΩ, $R_2 = 16.2$ kΩ, $R_4 = 1.6$ kΩ, $R_5 = R_6 = 5.1$ kΩ and $R_7 = R_8 = R_9 = R_{10} = 10$ kΩ.

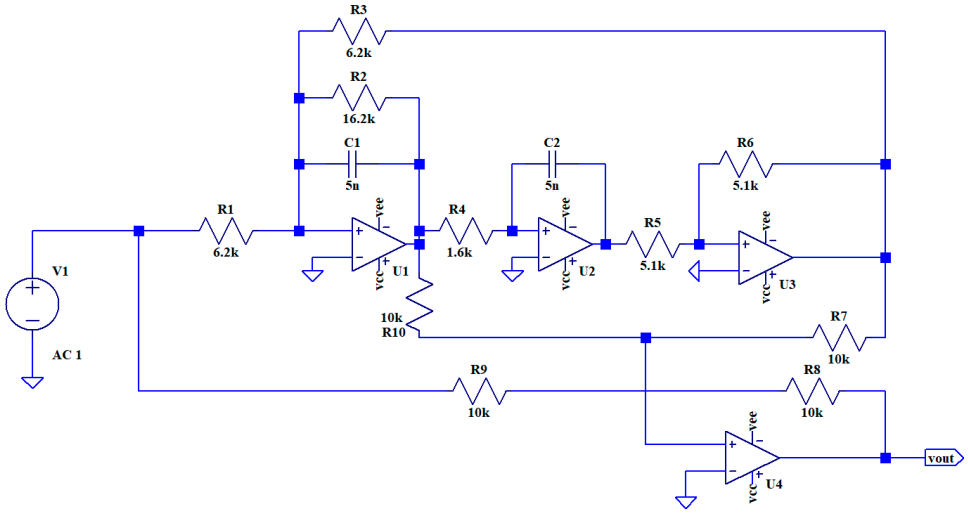


Figure 3. Schematic diagram of the fourth-order four-op-amp biquad high-pass filter.

The behavior of each biquad stage is controlled by the second-order high-pass transfer function, where K represents the passband gain, s represents the laplace variable which is used to analyze circuit behavior in the frequency domain, ω_0 represents the cutoff angular frequency of the filter and Q is the quality factor which measures the sharpness or selectivity of the filter's frequency response.

$$H(s) = \frac{Ks^2}{s^2 + (\frac{\omega_0}{Q})s + \omega_0{}^2} \,. \tag{2}$$

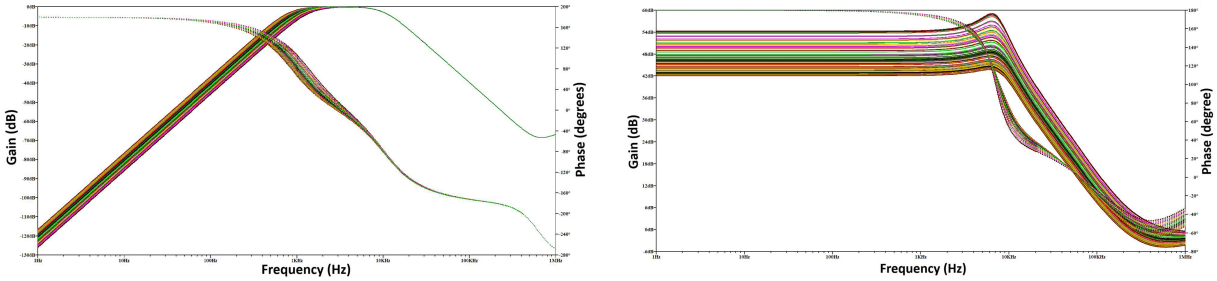
2.1.2. Fault Dictionary and Parametric Modeling

A fault dictionary was developed on the basis of the extensive circuit simulations performed in LTspice XVII to enable reliable analog fault diagnosis. This dictionary captures characteristics of both the fault-free circuit and various faulty states of the circuit, allowing subsequent comparison and identification of faults during testing.

Simulations included:

- Nominal operation (fault-free case) with components at their design values.
- Parametric (soft) faults, where individual passive components (resistors and capacitors) varied ±50% from their nominal values; this was intentionally chosen to assess the diagnostic framework under severe parametric drift conditions [12], although typical manufacturing tolerances for standard resistors and capacitors are generally within ±1% to ±10%. This allows the robustness of the proposed algorithm to be validated under boundary-level realistic failure conditions, rather than only under mild deviations.

AC frequency response analysis (magnitude and phase Bode plots) and transient responses are used as primary sources of fault signatures. Figures 4 and 5 show the simulation waveforms for the Sallen–Key bandpass filter and the four-op-amp biquad high-pass filter under parametric fault conditions [10]. Each colored line represents a separate Monte Carlo simulation run with randomly varied component values based on specified tolerances.



(**a**) Sallen–Key bandpass filter: Bode plot (**b**) Four-op-amp biquad high-pass filter: Bode plot

Figure 4. (**a**) Frequency response (magnitude and phase Bode plots) of the Sallen–Key bandpass filter (**left**) and the (**b**) four-op-amp biquad high-pass filter (**right**) under nominal and parametric fault conditions (±50% deviation).

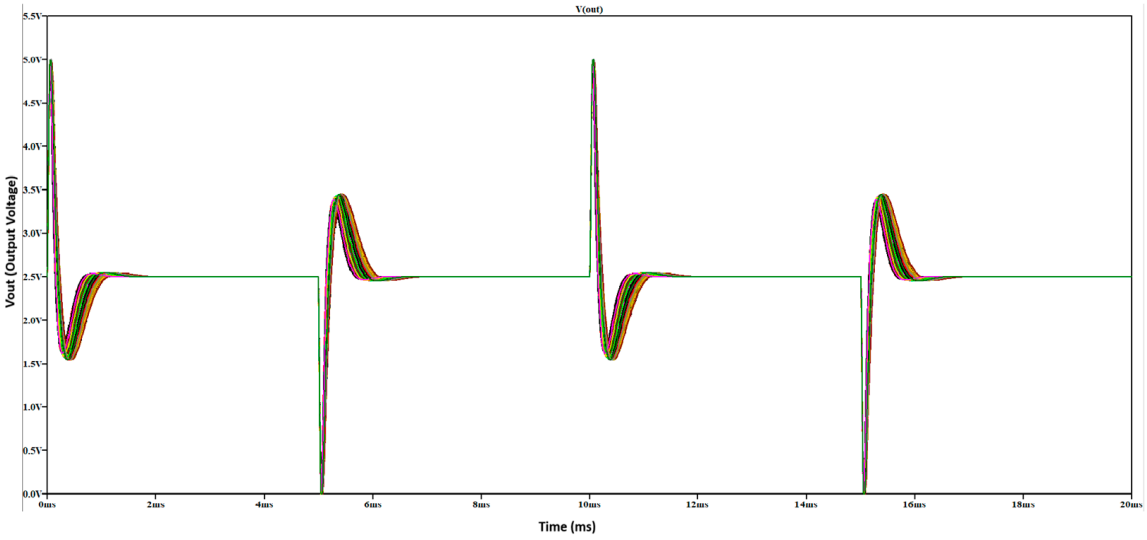


Figure 5. Transient pulse responses of both filter topologies (Sallen–Key bandpass and four-op-amp biquad high-pass) under parametric fault conditions (±50% deviation). Responses show similar qualitative behavior with minor amplitude and timing variations.

Figure 4 shows the frequency-domain signatures of both filters under nominal and ±50% fault conditions. The Sallen–Key BPF exhibits shifts in center frequency, peak gain, and bandwidth, while the biquad HPF shows cutoff frequency shifts and smoother transition slopes. Figure 5 shows the time-domain responses, where fault conditions produce minor amplitude and timing variations. Overall, frequency-domain features provide stronger fault discrimination, while time-domain features offer supporting information.

The various parametric fault classes that are considered for each filter circuit are explained in the tables below. These classes are the base of the fault dictionary and are generated through repeated Monte Carlo simulations, including both boundary conditions and intermediate values within the ±50% range.

2.2. Data Generation and Noise Stress Framework

A multi-stage data generation and noise-injection pipeline was designed to model how the circuit works under real-world conditions. By adding controlled noise to the simulated data, the models work even when there is an uncertainty in the measurements.

2.2.1. Monte Carlo Simulation and Large-Scale Dataset Construction

To account for inherent manufacturing tolerances and ensure statistical robustness, a synthetic dataset was constructed using Monte Carlo (MC) simulation [13].

For each fault class Fi defined in Tables 1 and 2, 200 statistically independent simulation runs were performed, with no correlation between successive samples. The MC simulation in LTspice follows a parametric direct random sampling approach, in which each non-faulty component value is independently drawn with equal probability from within its specified tolerance band, following a uniform probability distribution. This differs from Gaussian-weighted sampling or Markov Chain Monte Carlo methods. During each simulation run, only the non-faulty components are subjected to this variation, while the target faulty component remains fixed at its prescribed deviation, thereby ensuring that fault class labels remain unambiguous across all 200 runs.

Table 1. Fault dictionary—parametric faults (±50%) for the Sallen–Key bandpass filter.

Fault Class	Component	Type	Nominal Value	Faulty Value (±50%)
F_0	–	Nominal	All nominal	–
F_1	R_1	Soft	23 kΩ	11.5 kΩ/34.5 kΩ
F_2	R_2	Soft	11 kΩ	5.5 kΩ/16.5 kΩ
F_3	R_3	Soft	10 kΩ	5 kΩ/15 kΩ
F_4	R_4	Soft	10 kΩ	5 kΩ/15 kΩ
F_5	C_1	Soft	10 nF	5 nF/15 nF
F_6	C_2	Soft	10 nF	5 nF/15 nF
F_7	C_3	Soft	2.2 nF	1.1 nF/3.3 nF
F_8	C_4	Soft	1.1 nF	0.55 nF/1.65 nF

Table 2. Fault dictionary—parametric faults (±50%) for the 4-op-amp biquad high-pass filter.

Fault Class	Component	Type	Nominal Value	Faulty Value (±50%)
F_0	–	Nominal	All nominal	–
F_1	R_1	Soft	6.2 kΩ	3.1 kΩ/9.3 kΩ
F_2	R_2	Soft	16.2 kΩ	8.1 kΩ/24.3 kΩ
F_3	R_3	Soft	6.2 kΩ	3.1 kΩ/9.3 kΩ
F_4	R_4	Soft	1.6 kΩ	0.8 kΩ/2.4 kΩ
F_5	R_5	Soft	5.1 kΩ	2.55 kΩ/7.65 kΩ
F_6	R_6	Soft	5.1 kΩ	2.55 kΩ/7.65 kΩ
F_7	R_7	Soft	10 kΩ	5 kΩ/15 kΩ
F_8	R_8	Soft	10 kΩ	5 kΩ/15 kΩ
F_9	R_9	Soft	10 kΩ	5 kΩ/15 kΩ
F_{10}	R_{10}	Soft	10 kΩ	5 kΩ/15 kΩ
F_{11}	C_1	Soft	5 nF	2.5 nF/7.5 nF
F_{12}	C_2	Soft	5 nF	2.5 nF/7.5 nF

For every Monte Carlo run, the defective part was tested using a uniform distribution that was within ±50% of the mean:

$$X_faulty \sim U(0.5 \cdot X_0,\ 1.5 \cdot X_0)\,, \tag{3}$$

A Gaussian distribution centered around their nominal values was used to change all of the non-defective parts on their own:

$$X \sim N(X_0,\ (\sigma \cdot X_0)^2)\ , \tag{4}$$

where X_0 is the nominal value, and σ is the level of tolerance.

This process yielded a total balanced dataset of 1800 samples for the Sallen–Key filter (9 classes × 200 runs) and 2600 samples for the biquad filter (13 classes × 200 runs). The raw transient responses were captured at a uniform sampling frequency sufficient to satisfy the Nyquist–Shannon criterion for the highest-frequency components of interest.

2.2.2. Signal Preprocessing and Normalization

Before feature extraction, the raw signals from both transient and frequency-domain simulations were processed to make sure that all Monte Carlo runs were the same. The normalized signal x_{norm} is defined as follows:

$$x_{norm} = \frac{(x - x_{min})}{(x_{max} - x_{min})}. \quad (5)$$

where x is the original signal value, $x_{\min}$ is the minimum value of the signal, $x_{\max}$ is the maximum value of the signal, and x_{norm} is the normalized signal value. This step eliminates magnitude bias caused by different supply voltages between the two benchmark topologies.

LTspice was used to make each response $x(t)$ last for 10 ms for transient analysis. Measurement directives were used to get key signal characteristics. The steady-state value was checked at t = 9 ms to make sure the signal had settled down enough.

We did a frequency-domain analysis by sweeping an AC signal from 10 Hz to 1 MHz using a logarithmic scale with 100 points per decade. From the frequency response that came out, important features were taken out. The cutoff frequency was defined as the frequency at which the magnitude of the output voltage drops to 0.707 times the maximum gain.

2.3. Robustness Evaluation Under AWGN Corruption

To study how the model works under realistic conditions, additive white Gaussian noise (AWGN) was intentionally added to clean signals. Three distinct noise levels were selected to represent signals with different noise levels: 20 dB for mild noise, 10 dB for moderate noise, and 5 dB for severe noise.

The signal-to-noise ratio (SNR) in the decibel scale is defined as [11]

$$SNR_{dB} = 10\, log_{10}(\frac{P_{signal}}{P_{noise}}), \quad (6)$$

where P_{signal} represents the average power of the simulated transient response and P_{noise} denotes the power of the injected Gaussian noise.

Rearranging (6), the required noise power for a desired SNR level is calculated as

$$P_{noise} = \frac{P_{signal}}{10^{\frac{SNR_{dB}}{10}}}. \quad (7)$$

Thus, the corrupted signal is expressed as

$$x(t) = s(t) + n(t), \quad (8)$$

where $s(t)$ and $n(t)$ represent the clean transient response and the additive noise signal, respectively, with $n(t) \sim \mathrm{N}(0, \sigma^2)$ denoting zero-mean white Gaussian noise whose variance corresponds to P_{noise}.

Mathematical Justification of Exponential Noise Growth

From (7), it is evident that

$$P_{noise} \alpha\ 10^{-\frac{SNR_{dB}}{10}}. \quad (9)$$

This relationship indicates that noise power varies exponentially with respect to SNR (in dB scale). A linear decrease in SNR produces an exponential increase in injected noise power.

For illustration:

- At 20 dB: $P_{noise} = \frac{P_{Signal}}{100}$.
- At 10 dB: $P_{noise} = \frac{P_{Signal}}{10}$.
- At 5 dB: $P_{noise} = \frac{P_{Signal}}{3.162}$.

As the noise intensity is reduced from 20 dB to 10 dB, the noise power also increases by a factor of 10. When we reduce it further from 10 dB to 5 dB, the noise power is increased by 3.16 times. This exponential amplification of noise power as the noise intensity reduces explains why the transient response waveforms in the figure look distorted as the noise intensity reduces. As can be seen in Figure 6, the 20 dB waveform preserves most of the features from the clean signal, whereas the 5 dB one looks very much distorted. This multi-level stress testing framework helps to understand how the classifier's performance degrades under realistic conditions.

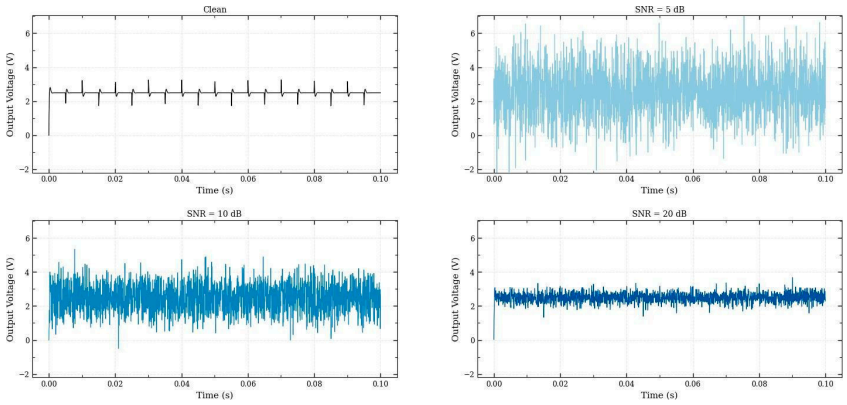


Figure 6. Representative transient responses for a faulty state under clean, 5 dB, 10 dB, and 20 dB SNR conditions.

As shown in the Figure 6, it can be seen that the 20 dB condition retains most of the original structure of the transient response, whereas the 10 dB case introduces visible disturbances. At 5 dB, the noise becomes dominant, and the original waveform structure is largely distorted Figure 7.

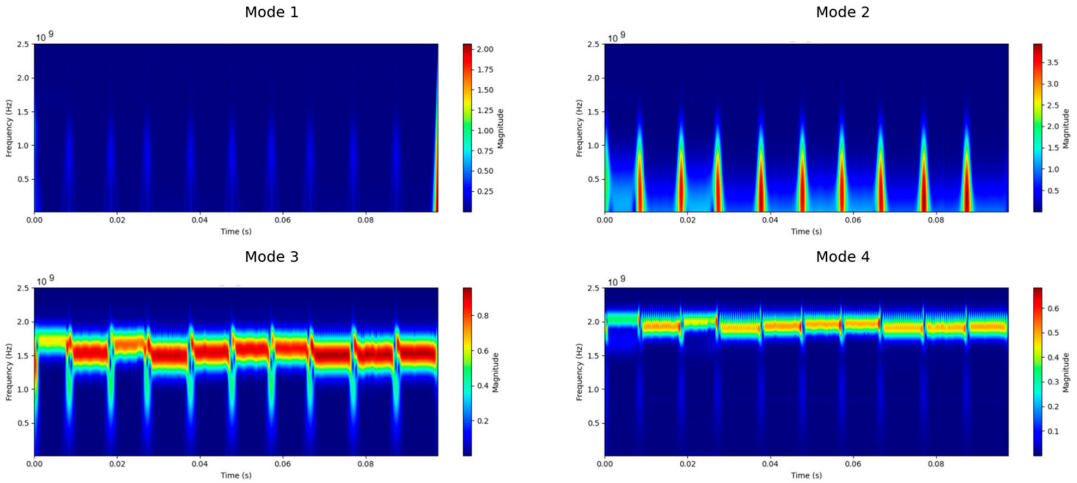


Figure 7. Continuous Wavelet Transform (CWT) scalograms of the four Variational Mode Decomposition (VMD) modes, highlighting the time–frequency characteristics captured by each mode.

This multi-level stress testing framework provides a quantitative measure of classifier performance degradation and ensures realistic validation under simulated noisy conditions.

2.4. Advanced Signal Decomposition and Feature Extraction

2.4.1. Variational Mode Decomposition (VMD)

Variational Mode Decomposition (VMD) decomposes the transient signal $f(t)$ into K band-limited sub-signals (IMFs) by solving the constrained variational problem.

The VMD parameters for this study are: $K = 4$ modes, penalty factor $\alpha = 2000$ (which controls the bandwidth of each mode), noise tolerance $\tau = 0$, DC component disabled ($DC = 0$), initialization done by evenly distributing the frequencies of the modes ($init = 1$), and convergence tolerance $\epsilon = 1 \times 10^{-7}$. The VMD implementation employs the algorithm developed by Dragomiretskiy and Zosso [14], as executed within the Python 3.13 *vmdpy* library.

2.4.2. Continuous Wavelet Transform (CWT) and Scalograms

The CWT maps a one-dimensional signal into a two-dimensional time–frequency representation. The resulting wavelet coefficients from the scalogram are converted into magnitude scalograms by taking the absolute value, enabling clear visualization and analysis of signal energy distribution across time and frequency.

The PyWavelets (pywt) library in python is used to implement the CWT in this work. The complex Morlet wavelet is chosen as the mother wavelet, as it is good for balancing between time and frequency localization. The equation for the complex Morlet wavelet is given below, where $\psi(t)$ denotes the wavelet function, t represents time, ω_0 is the central frequency, e^{-t^2} defines the Gaussian envelope, and $e^{j\omega_0 t}$ represents the complex sinusoidal carrier.

$$\psi(t) = \frac{1}{\sqrt{\pi}} e^{-t^2} \; e^{(j\omega_0 t)}. \tag{10}$$

The transform is calculated over a limited number of scales, which are defined as s = 1, 2, …, 128, with the highest scale being 128. The sampling period for the CWT calculation comes directly from the time-domain signal, where $\Delta t = t_{i+1} - t_i$. This makes sure that the simulation data is consistent.

From the CWT representation, a set of statistical features is extracted to characterize the signal. The dominant frequency is identified as the frequency corresponding to the scale with the maximum aggregated coefficient magnitude across time.

2.4.3. Hierarchical Feature Fusion and Statistical Vector Construction

To get a high-dimensional statistical feature vector, classic features of physical circuits that cover multiple domains are combined. This combination lets the classification model see both gradual changes in performance on a macro level and sudden changes on a micro level. The final feature vector is formed by combining three different groups:

1. **Time-Domain Features:** Transient parameters including peak voltage (V_p), rise time (t_r), fall time (t_f), and settling time (t_s).
2. **Frequency-Domain Features:** Derived characteristics such as cutoff frequency (f_c), bandwidth (BW), passband ripple, and peak gain.
3. **IMF-level Statistical Features:** To evaluate the signal complexity at each decomposition level, five statistical measures are extracted from each of the intrinsic mode functions (IMFs) obtained through VMD [14,15]:

- Arithmetic mean (μ);
- Standard deviation (σ);
- Shannon entropy (H);

- Energy (E);
- Maximum amplitude (Max).

The resulting 20-dimensional statistical sub-vector (5 features × 4 IMFs) is integrated with the existing time and frequency features to create a final feature vector.

2.5. Machine Learning Classification Framework

The diagnostic engine is developed through a structured evaluation of four classification frameworks. Each model was developed to overcome the limitations caused by the previous model, improving their accuracy further.

2.5.1. Support Vector Machine (SVM)—The Initial Baseline

The SVM was used as the baseline classifier. With 5-fold internal cross-validation, grid search optimization used C ∈ {10, 50, 100} and $\gamma \in \{0.01, 0.05, 0.1\}$, where C is the regularization parameter which controls the trade-off between margin size and classification errors and γ is the RBF kernel parameter. The data was split into two groups: 70% for training and 30% for testing. StandardScaler was required to normalize the RBF kernel sensitivity. The one-versus-rest (OVR) decision function was used to classify multiple classes. While SVM works well against high-dimensional data, it has lower accuracy due to its sensitivity to statistical features.

2.5.2. Random Forest (RF)—Ensemble Averaging

To further improve the classification performance beyond SVM, the Random Forest method was applied. The RF classifier used 300 decision trees with no depth limit. StandardScaler was used to scale the features in a scikit-learn pipeline so that data would not leak between folds. The model used n_jobs = -1 for parallel processing and random_state = 42 to make sure the results were the same each time. The final predicted class is obtained using majority voting across all trees, which helps reduce the variance (σ^2) associated with individual circuit simulations.

RF provided more improved performance than SVM by capturing the non-linear interactions between the mean, energy, and entropy features of the four IMFs.

2.5.3. Gradient Boosting Classifier (GBC)—Sequential Refinement

The third stage of improvement involved gradient boosting. The implementation used 300 sequential estimators and a learning rate of 0.05 to avoid overfitting. The maximum depth of the tree was 3 levels (max depth = 3), and the minimum number of samples per split and leaf was 2 and 1, respectively. It is an additive model that minimizes a differentiable loss function L by sequentially adding weak learners hm(x) [16]:

$$F_m(x) = F_{m-1}(x) + \nu\gamma_m h_m(x), \tag{11}$$

where $F_m(x)$ represents the ensemble model obtained at iteration m, while $F_{m-1}(x)$ corresponds to the model from the previous iteration. The term $h_m(x)$ denotes the m-th weak learner (commonly a decision tree), γ_m indicates the step size that determines the learner's contribution, and ν is the learning rate that regulates the magnitude of the update [16,17]. By focusing on the hard-to-classify samples from the 200-run Monte Carlo sets, GBC outperformed RF by refining the decision boundaries for closely overlapping parametric fault classes.

2.5.4. Proposed Heterogeneous Stacking Ensemble

The final stage of the diagnostic framework is a two-tier **stacking ensemble** [18,19]. This architecture treats the class probabilities generated by the Level-0 learners (SVM,

RF, GBC, and Extra Trees) as meta-features. A Logistic Regression meta-learner, optimized via the L-BFGS solver, computes the final prediction using a softmax-based probability distribution:

$$P(y = k \mid p) = \frac{exp(\beta_k \cdot p)}{\Sigma_{j=1}^{K} exp(\beta_j \cdot p)}, \quad (12)$$

where **p** represents the vector of base-model probabilities and $P(y = k \mid p)$ is the probability that the input sample belongs to class k, y is the predicted output class (fault category), k is a particular class among the K possible classes, β_k is the weight vector learned by the Logistic Regression meta-learner for class k, K is the total number of fault classes. This fusion allowed the framework to achieve peak accuracies of **97% and 94%**, as the meta-learner effectively corrects the individual model biases.

2.5.5. Training and Validation Strategy

To ensure the integrity of the diagnostic results and eliminate data leakage, a strict validation protocol was maintained:

- **Outer Loop (5-Fold Stratified Cross-Validation):** The dataset was split into five stratified folds, and the class distribution was the same in each one. Each fold was used as a test set over and over again, and the other folds were used as a training set. The accuracy that was reported is the average performance across these outer folds.
- **Inner Loop (5-Fold Cross-Validation for Meta-Feature Generation):**
- Within each outer training split, an extra stratified 5-fold cross-validation was done to get Out-of-Fold (OOF) predictions from the base learners. Four folds were used to train each base model, and the last fold was used to test it. The predicted class probabilities from these validation folds were combined to make the OOF meta-feature matrix.
- **Meta-Learner Training:** The Logistic Regression meta-learner was trained only on the OOF meta-features that came from the inner loop. This makes sure that the stacking layer only gets predictions from data that it has not seen before.
- **Final Evaluation on Outer Test Set:** After making OOF features, base learners were trained again on the whole outer training set and then used to make probability predictions for the outer test set. The trained meta-learner then used these predictions to make final classifications.

3. Ablation Study

A thorough ablation study was performed on two analog filter circuits, the Sallen–Key bandpass filter and the biquad filter, to systematically evaluate the contribution of each feature domain and their synergistic effect. We looked at seven different combinations of features: time domain (TD) only, frequency domain (FD) only, intrinsic mode function (IMF) only, TD + FD, TD + IMF, FD + IMF, and the full TD + FD + IMF set. All experiments adhered to a uniform 5-fold cross-validation protocol.

3.1. Interpretation

Adding FD to TD gives all classifiers a small boost, as seen in Figures 8 and 9. This shows that spectral information works well with temporal statistics. IMF features alone are not as strong as FD, but when they are combined with either TD or FD, they make performance much better. This shows that VMD-derived components capture fault-specific dynamics that are not in the raw domain.

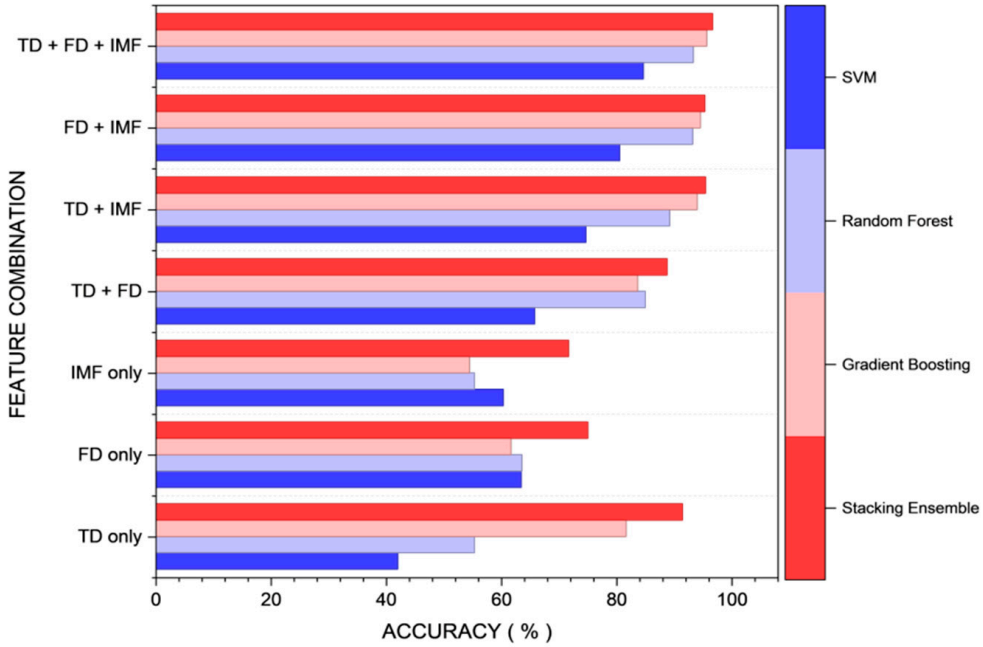


Figure 8. Ablation study results for the Sallen–Key bandpass filter.

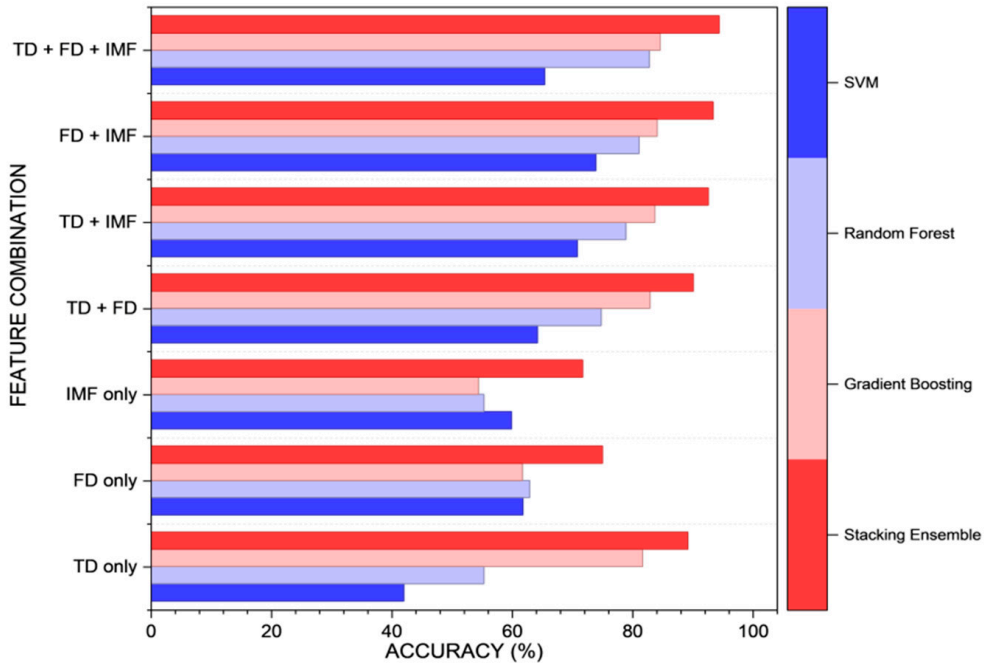


Figure 9. Ablation study results for the biquad filter.

The full feature set (TD + FD + IMF) always gives the best results. The stacking ensemble gets 96.67% accuracy and macro-F1 in the Sallen–Key BPF and 94.4% in the biquad filter. Adding IMF to TD makes Random Forest and Gradient Boosting work the best, with accuracy increases of about 9% and 12%, respectively, in the Sallen–Key BPF and similar gains in the biquad filter. This shows that they can take advantage of the richer representation.

The study shows that multi-domain feature engineering is necessary for accurate fault classification and that the ensemble strategy makes the best use of the three feature groups' complementary information.

3.2. Key Findings and Generalization

The highest classification accuracy was seen in both circuits when a combination of time-domain (TD), frequency-domain (FD), and intrinsic mode function (IMF) features was used. The steady shift from using a single type of feature to combining all of them shows the importance of feature fusion. In particular, IMF features make a significant difference when used with TD or FD features, since they capture details that the basic signal characteristics miss. At the same time, the low variation in results for the full feature set indicates that this approach is not only accurate but also stable and reliable.

4. Experimental Results and Diagnostic Performance

4.1. Case Study I: Sallen–Key Bandpass Filter

4.1.1. Performance Comparison Across Different Models

The metrics from the confusion matrix are used to evaluate the performance of the proposed methodology to view its efficiency; the metrics include precision (Pr), recall (Re), and F1-score (F_1). These parameters are mathematically defined as

$$Precision\ (Pr) = \frac{TP}{TP + FP}, \tag{13}$$

$$Recall\ (Re) = \frac{TP}{TP + FN}\ , \tag{14}$$

$$F1\text{-}score\ (F_1) = 2 \times \frac{Pr \times Re}{Pr + Re}, \tag{15}$$

$$Accuracy(\%) = \frac{TP + TN}{TP + TN + FP + FN} \times 100, \tag{16}$$

where TP, TN, FP, and FN denote true positives, true negatives, false positives, and false negatives, respectively.

The diagnostic performance is evaluated by comparing four different classification models. Table 3 metrics helps us to view the transition from the basic SVM model to the proposed stacking ensemble.

Table 3. Diagnostic performance metrics across different models (Sallen–Key BPF).

Model	Precision	Recall	Macro-F1	Accuracy (%)
Tuned SVM (RBF)	0.81	0.78	0.78	78.15
Random Forest (RF)	0.94	0.94	0.94	93.70
Gradient Boosting (GB)	0.94	0.95	0.94	94.00
Stacking Ensemble	**0.97**	**0.97**	**0.97**	**96.67**

Bold values indicate the best performing model across all metrics.

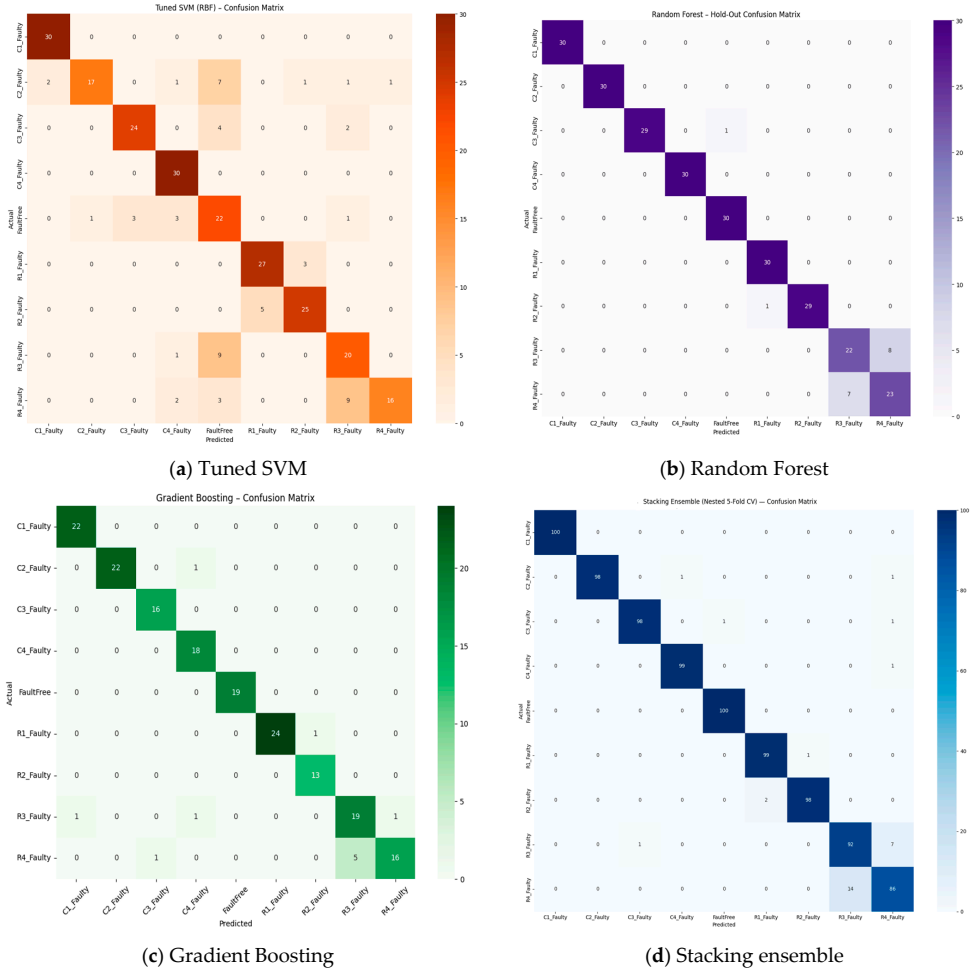
The basic tuned SVM model achieved an accuracy of 78.15% with optimized parameters (C = 50, γ = 0.05). However, it is less effective in handling the complex non-linear relationships present in the statistical features and also particularly this model had difficulty in distinguishing the series-branch components R_3 and R_4, which generate nearly identical output responses for parametric variations.

Random Forest significantly improved the performance, reaching an accuracy of 93.70% by effectively modeling non-linear relationships among the mean, energy, and entropy features extracted from the four IMFs. Gradient Boosting provided a slight additional improvement, achieving 94.00% accuracy by refining the decision boundaries and focusing more strongly on difficult samples.

The stacking ensemble combined the strengths of all base learners and achieved the highest performance, with an average cross-validation accuracy of 96.67% with a standard

deviation of 1.14%. This approach also improved the classification among challenging components R_3 and R_4 by increasing their F1-scores to 0.89 and 0.88, respectively, values that were considerably low with the baseline SVM. Similarly, the capacitors C_1 and C_2 consistently achieved perfect F1-scores of 1.00 across all models, likely because the feedback node between them enables the VMD-based features to capture their individual effects more distinctly.

The improvements across models can be viewed through the confusion matrices shown in Figure 10. These matrices show a gradual reduction in misclassifications, progressing from the relatively scattered predictions of the SVM to the clearer classification patterns produced by Random Forest and Gradient Boosting, and this leads to the improved accuracy observed in the stacking ensemble.



(**a**) Tuned SVM (**b**) Random Forest

(**c**) Gradient Boosting (**d**) Stacking ensemble

Figure 10. Comparative confusion matrices for Sallen–Key BPF across four diagnostic models. The transition (**a**–**d**) illustrates the progressive reduction in fault ambiguity.

4.1.2. Topological Analysis of Series-Branch Ambiguity

In Figure 2, R_3 and R_4 are connected in a direct series branch between the output of the first operational amplifier stage and the non-inverting input of the second stage. Crucially, there is no intermediate node between R_3 and R_4 that is accessible at the circuit output. As a result, the voltage divider formed by R_3 and R_4 collectively determines the signal amplitude reaching the non-inverting input of the second stage, while the individual contributions of R_3 and R_4 cannot be independently resolved from the single output measurement point used in this study.

From a transfer function perspective, R_3 and R_4 appear in the denominator of the second-stage gain expression as a combined series resistance (R_3 + R_4). Consequently,

variations in either resistor produce mathematically identical shifts in key characteristics such as the 3 dB cutoff frequency, passband gain, and transient rise time under the ideal single-measurement-point observation model. This condition gives rise to what is formally termed an *unobservable fault pair* with respect to the selected output node. This topologically inherent ambiguity is addressed by merging R_3 and R_4 into a single compound fault class.

Since R_3 and R_4 generate identical output signal characteristics under the single-output measurement scheme, their intrinsic mode function (IMF) feature vectors are statistically indistinguishable, except for minor variations introduced by Monte Carlo Gaussian component tolerances.

4.1.3. Statistical Stability and Validation

The final stacking ensemble model is validated using a stratified five-fold cross-validation to ensure statistical stability [13]. Figure 11 plots the accuracy across each fold. The standard deviation of 1.14% across these folds shows that this model performs better with the Monte Carlo dataset, which has more unpredictable features. The fault-free class achieved a perfect 1.00 precision and recall, ensuring the system possessed a zero-false-alarm rate.

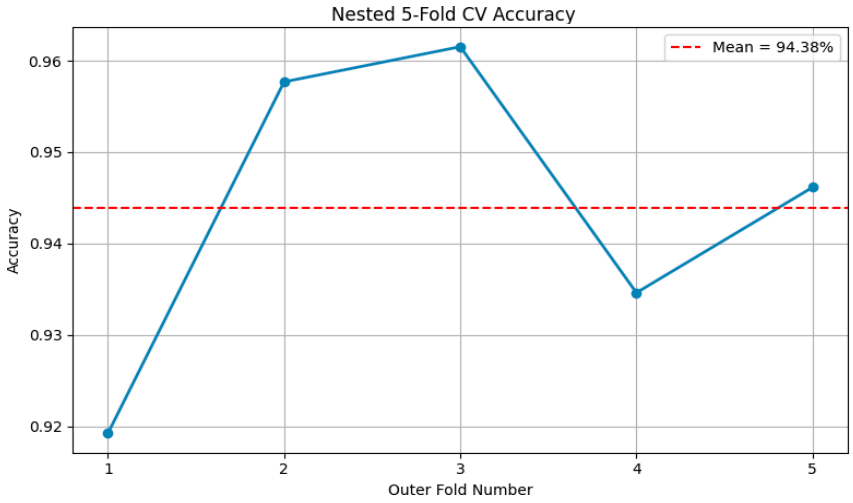


Figure 11. Classification accuracy across 5-fold cross-validation, demonstrating model robustness.

4.2. Case Study II: Four-Op-Amp Biquad High-Pass Filter

4.2.1. Performance Comparison Across Different Models

The biquad HPF has more complexity due to the large number of components which involve 13 different classes (12 fault classes and one fault-free class). The performance of the models is evaluated using the metrics derived from the confusion matrix—including precision (*Pr*), recall (*Re*), F1-score (F_1), and accuracy (*Acc*)—as per Equations (13), (14), (15), and (16), respectively. Table 4 metrics helps us to view the performance gap between the basic SVM model and the proposed stacking ensemble.

Table 4. Diagnostic performance metrics across different models (biquad HPF).

Model	Precision (*Pr*)	Recall (*Re*)	Macro-F_1	Accuracy (%)
Tuned SVM (RBF)	0.67	0.65	0.65	65.38
Random Forest (RF)	0.83	0.83	0.83	82.82
Gradient Boosting (GB)	0.85	0.85	0.85	84.62
Stacking Ensemble	**0.95**	**0.94**	**0.94**	**94.38**

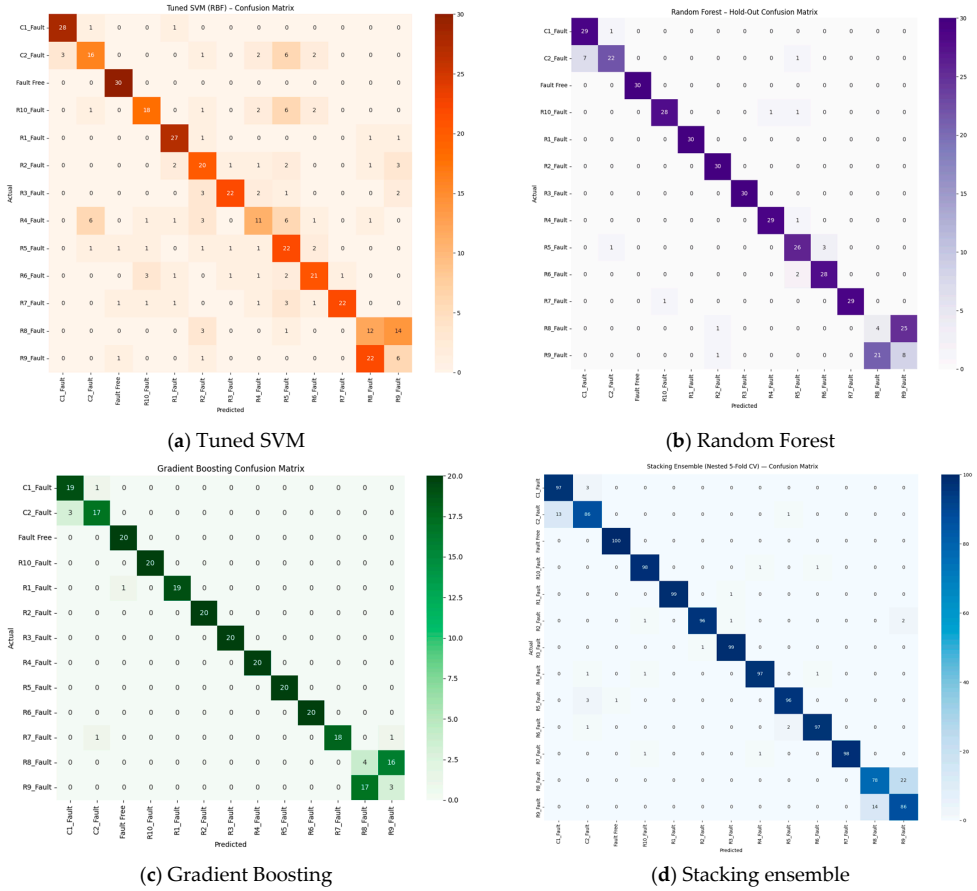
Bold values indicate the best performing model across all metrics.

The basic tuned SVM struggled to handle the high-dimensional features of the biquad circuit, achieving an accuracy of only 65.38% despite using optimized parameters ($C = 50$, $\gamma = 0.05$). A major difficulty in this topology arises from the strong similarity between the R_8 and R_9 fault classes. These components are located in the feedback loops of the biquad structure, where it produces similar damping and gain characteristic output for most of the parametric variations. As a result, their fault signatures become extremely similar, making them difficult to distinguish using a single kernel-based classifier.

Random Forest improved the overall accuracy to 82.82% by modeling complex non-linear relationships among the statistical features extracted from the IMFs. Gradient Boosting provided an additional improvement, reaching up to 84.62% accuracy by refining the decision boundaries and by giving greater importance to previously misclassified samples. However, both approaches continued to struggle with the R_8–R_9 ambiguity, with F1-scores remaining as low as 0.20 and 0.15 respectively in the Gradient Boosting model, making this pair the most challenging fault combination in the study.

The stacking ensemble combined the strengths of all base learners and along with the Logistic Regression meta-learner it achieved the highest performance with average accuracy of 94.38% and a standard deviation of 2.1%. Importantly, it improved the classification of the difficult R_8 and R_9 faults, increasing their F1-scores to 0.75 and 0.74 respectively. This shows that the stacking ensemble model is able to capture subtle non-linear decision boundaries that are often missed by individual models.

For the remaining fault classes as it can be seen in Figure 12, the integration capacitors C_1 and C_2 and the frequency-determining resistors R_1–R_{10} were classified reliably across all models because their fault signatures remain sufficiently distinct even within the more complex 13-class classification.



(**a**) Tuned SVM (**b**) Random Forest

(**c**) Gradient Boosting (**d**) Stacking ensemble

Figure 12. Comparative confusion matrices for biquad HPF across four diagnostic models, illustrating the reduction in fault ambiguity (**a**–**d**).

4.2.2. Topological Analysis of the R_8–R_9 Ambiguity Zone

The R8–R9 fault class ambiguity in the four-op-amp biquad high-pass filter, which arises from their closely related roles within the feedback network of the final op-amp stage, is topologically more subtle than the R3–R4 case but follows the same underlying physical logic. As seen in Figure 3, both resistors are connected at the inverting summing node, which functions as a weighted summing amplifier and jointly controls the damping factor and quality factor (Q) of the filter through balanced resistor ratios. A deviation in R8 modifies the forward signal contribution from the previous stage, whereas a deviation in R9 alters the feedback strength and loop gain. Despite originating from different signal paths, both faults produce nearly identical changes in the observable output response, resulting in similar shifts in cutoff frequency and gain characteristics. Since the extracted diagnostic features are primarily derived from transient responses and VMD, they remain largely insensitive to subtle phase differences that distinguish the two faults. Consequently, individual classifiers show poor separability between R8 and R9. The stacking ensemble improves discrimination by combining complementary decision boundaries from multiple base learners, increasing F1-scores significantly. However, the improvement remains inherently limited. This indicates that the ambiguity is primarily caused by topological response similarity rather than model inadequacy, suggesting that additional measurements or alternative excitation signals would be required for complete fault separation.

4.2.3. Statistical Stability and Validation

The final stacking ensemble model is validated using a stratified five-fold cross-validation. Figure 13 plots the accuracy across each fold, demonstrating that this model performs better with the Monte Carlo dataset, which has more unpredictable features. The system maintained a perfect 1.00 *Pr* and *Re* for the fault-free class, ensuring a zero-false-alarm rate.

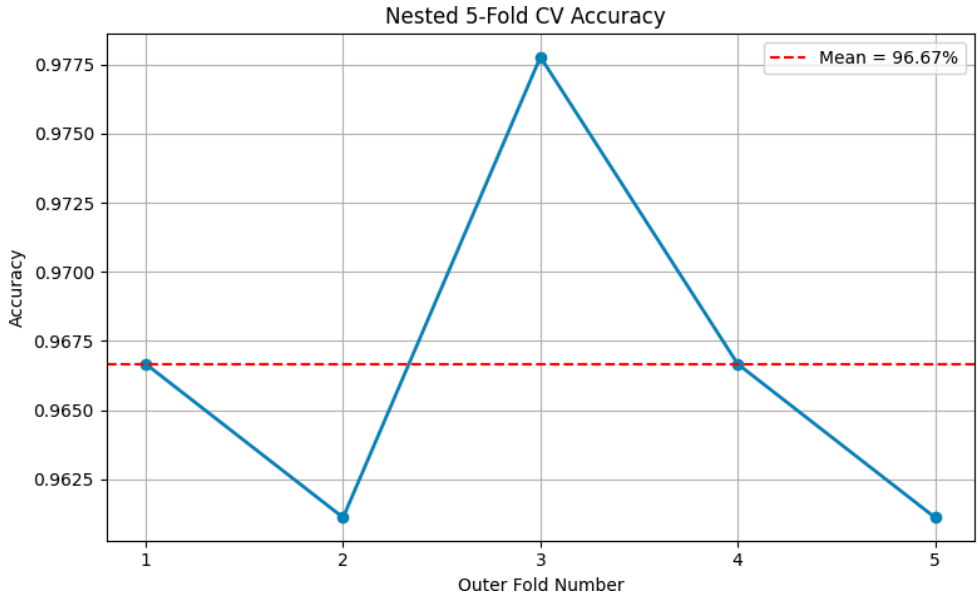


Figure 13. Classification accuracy across 5-fold cross-validation for the biquad HPF, demonstrating model robustness.

5. Noise Robustness and Signal Integrity Analysis

Under non-ideal conditions the reliability of the diagnostic framework is evaluated using a comparative signal integrity analysis. The primary goal is to quantify the preservation of discriminative numerical features within the VMD-based data arrays when additive white Gaussian noise (AWGN) is introduced.

5.1. Methodology for Noise Impact Assessment

This analysis follows a standardized numerical pipeline implemented in Python. The impact of the noise is quantified using the mean squared error (*MSE*), which then measures the difference between the clean and noisy feature arrays [20,21].

The methodology is defined by the following stages:

1. **Data Loading:** The intrinsic mode functions (IMFs) are loaded as numerical arrays from '.npy'/'.npz' files.
2. **Dynamic Range Enhancement:** To handle the varying scales of the VMD output, a log-transformation is applied: $f(x) = ln(1+|x|)$.
3. **Z-score Normalization:** To ensure the *MSE* is not biased by signal amplitude, each array is normalized to zero mean and unit variance: $\hat{I} = \frac{I-\mu}{\sigma+\epsilon}$.
4. **Metric Computation:** The *MSE* is calculated between the processed "clean" array (I_c) and the "noisy" version (I_n) at *SNR* = 20, 10, and 5 dB:

$$MSE = \frac{1}{N}\sum_{i=1}^{N}(I_c(i) - I_n(i))^2 \quad (17)$$

5.2. Performance Analysis of Sallen–Key BPF Under Noisy Conditions

The stability of the fault diagnosis system was evaluated by introducing noise at three levels: 20 dB (mild noise), 10 dB (moderate noise), 5 dB (severe noise) [22]. The following observations emphasize how the noise impacts the quality across different IMF levels and the variation in their classification performance.

IMF-Wise Noise Impact

The relationship between signal-to-noise ratio (SNR) and the mean squared error (MSE) across different intrinsic mode functions (IMFs) is shown in Figures 14 and 15.

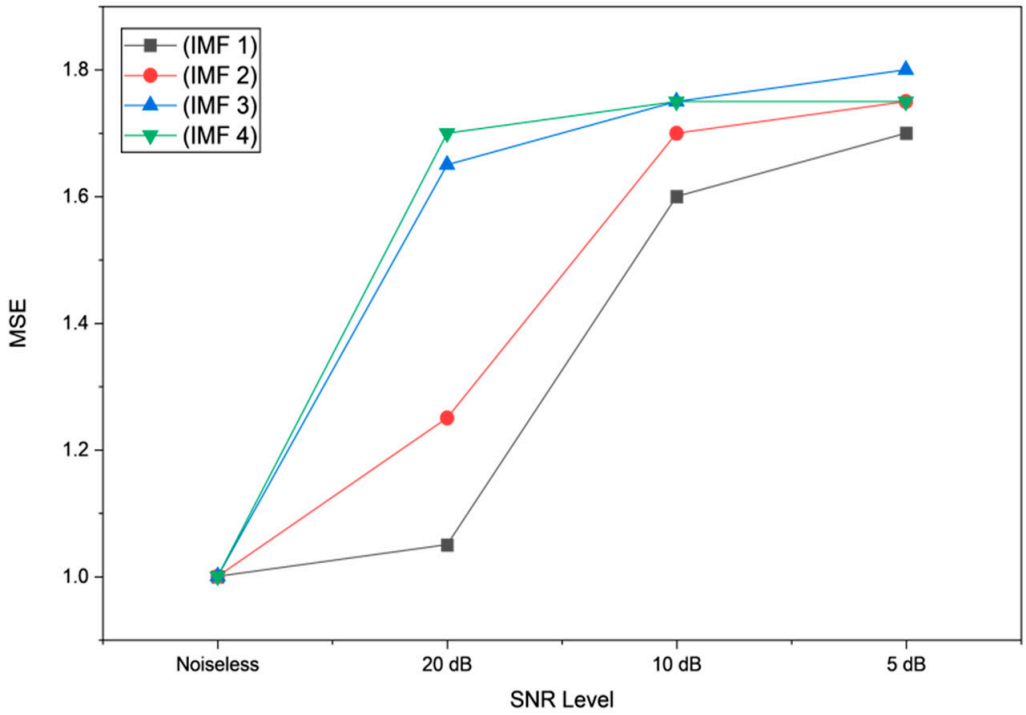


Figure 14. IMF-wise noise impact across noise levels.

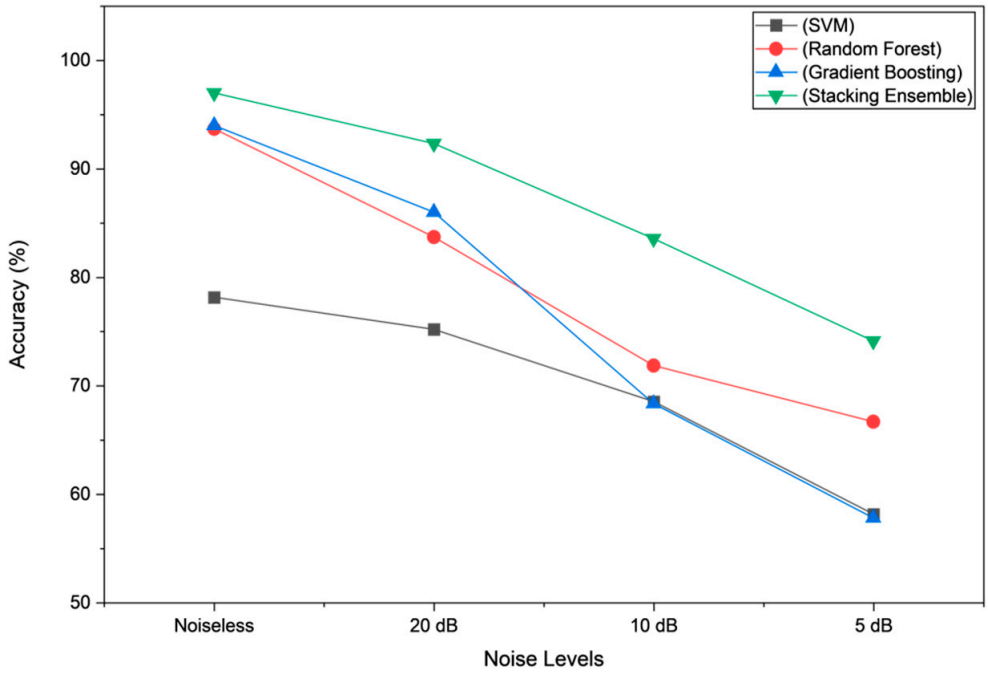


Figure 15. Classification accuracy of Sallen–Key BPF under varying noise levels.

As shown in Table 5, as the noise level increases, the IMFs exhibit divergent sensitivity patterns, which directly explain the curve crossings observed in these figures. At low noise levels (20 dB), all IMFs maintain relatively low MSE values, and their corresponding curves remain closely spaced, indicating that the signal structure is well preserved across all decomposition modes. However, below 10 dB, particularly for IMF1, which captures fine-grained fault signatures, the degradation becomes more pronounced compared with lower-frequency IMFs such as IMF3 and IMF4, which retain discriminative information for longer. This differential degradation causes the MSE curves to intersect at specific SNR thresholds, reflecting a reversal in the relative noise sensitivity of individual IMF bands. This behavior is topology-dependent. In the biquad filter, the multi-integrator structure channels fault energy into specific IMFs, resulting in more abrupt curve crossings. In contrast, in the Sallen–Key filter, fault energy is distributed more uniformly, producing smoother transitions. **Sensitivity of IMF1:** IMF1 consistently exhibits the minimum MSE at 20 dB, indicating that it effectively captures the dominant oscillatory behavior of the signal. However, it also shows the steepest increase in MSE when the SNR decreases to 10 dB, which directly contributes to the crossing behavior observed in Figure 14.

Table 5. Average MSE across IMFs for varying SNR levels (Sallen–Key BPF).

SNR Level	IMF1	IMF2	IMF3	IMF4
20 dB (Low Noise)	≈1.05	≈1.25	≈1.65	≈1.70
10 dB (Med Noise)	≈1.60	≈1.70	≈1.75	≈1.75
5 dB (High Noise)	≈1.70	≈1.75	≈1.80	≈1.75

Saturation at Lower Frequencies: For IMF3 and IMF4, the MSE curves corresponding to 10 dB and 5 dB tend to converge, indicating a saturation point at which noise energy dominates these lower-frequency components. This explains why the curves intersect and subsequently run nearly parallel under severe noise conditions.

5.3. Classifier Robustness Analysis of Sallen-Key BPF

The stacking ensemble consistently shows better noise resistance in both circuit topologies as mentioned in Table 6. The Sallen–Key BPF ensemble gets 97% accuracy when there is no noise, and only drops to 94.38% when there is 20 dB of noise. This shows that it is very resistant to mild noise. The difference in performance between the ensemble and the individual classifiers gets bigger as the noise level goes up. At 10 dB, where traditional models like SVM, Random Forest, and Gradient Boosting all have about the same level of accuracy (68–72%), the stacking ensemble has a much higher level of accuracy (83.56%). The ensemble still has 74.11% accuracy even when there is a lot of noise (5 dB), which is much better than the other models, which drop to much lower accuracy levels.

Table 6. Classification accuracy under different noise levels (Sallen–Key BPF).

Condition	SVM	RF	GB	Stacking
Noiseless	78.15	93.70	94.00	97.00
20 dB	75.19	83.70	86.00	92.33
10 dB	68.52	71.85	68.33	83.56
5 dB	58.15	66.67	57.78	74.11

5.4. Performance Analysis of Biquad HPF Under Noisy Conditions

The reliability of the four-op-amp biquad high-pass filter (HPF) was verified by using the same noise intensity levels (20 dB, 10 dB, 5 dB). The topology of biquad filter is more complex than the Sallen–Key bandpass filter; therefore, it shows different decomposition characteristics.

Results of Biquad Noise Impact

The impact of noise on the intrinsic mode decomposition of biquad filter signals is summarized in Table 7 and Figure 16.

Table 7. Average MSE across IMFs for varying SNR levels (biquad HPF).

SNR Level	IMF1	IMF2	IMF3	IMF4
20 dB (Low Noise)	≈0.01	≈0.12	≈0.52	≈1.13
10 dB (Med Noise)	≈0.23	≈1.37	≈1.58	≈1.50
5 dB (High Noise)	≈0.50	≈1.62	≈1.67	≈1.59

- **Low-Noise Precision:** The biquad filter maintains exceptionally low MSE (0.01) in IMF1 at a 20 dB level. This indicates that high-frequency fault components are better preserved than the Sallen–Key configuration.
- **Rapid Error Escalation:** The biquad HPF shows a very sharp increase in MSE at IMF2 when the noise is increased to 10 dB. This indicates that the characteristics of the biquad filter are affected by moderate levels of noise interference.
- **High-Frequency Robustness:** Among all fault types, it is observed that IMF1 is the most robust source, with MSE always less than 0.6, even at the highest noise level of 5 dB.

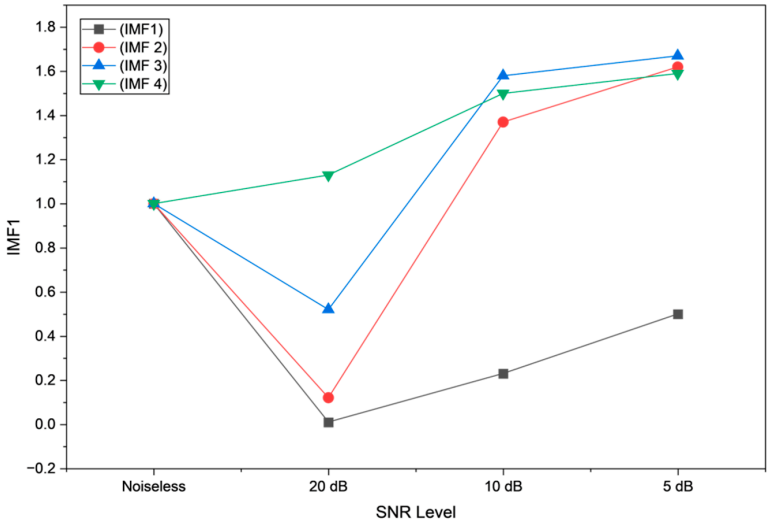


Figure 16. IMF-wise noise impact for four-op-amp biquad HPF.

5.5. Classifier Robustness Analysis of Biquad HPF

Similar behavior to the Sallen–Key BPF is observed in the biquad HPF, but the degradation is worse because the circuit has a multi-stage topology that makes noise louder across stages, as can be seen in Table 8 and Figure 17. The stacking ensemble gets 94.39% right when there is no noise and 83.85% right when there is 20 dB of noise. The other classifiers drop to the low 70% range. All models' performance drops sharply at 10 dB, but the ensemble still has a clear lead at 69.23%, while the other classifiers are only around 54–57%. Under very bad conditions (5 dB), all methods have a hard time classifying, but the stacking ensemble still gets the best accuracy of 56.15%, which is a big difference from the others.

Table 8. Classification accuracy under different noise levels (biquad HPF).

Condition	SVM	RF	GB	Stacking
Noiseless	65.38	82.82	84.62	94.38
20 dB	62.56	72.31	71.54	83.85
10 dB	55.13	56.92	53.85	69.23
5 dB	44.62	45.90	45.00	56.15

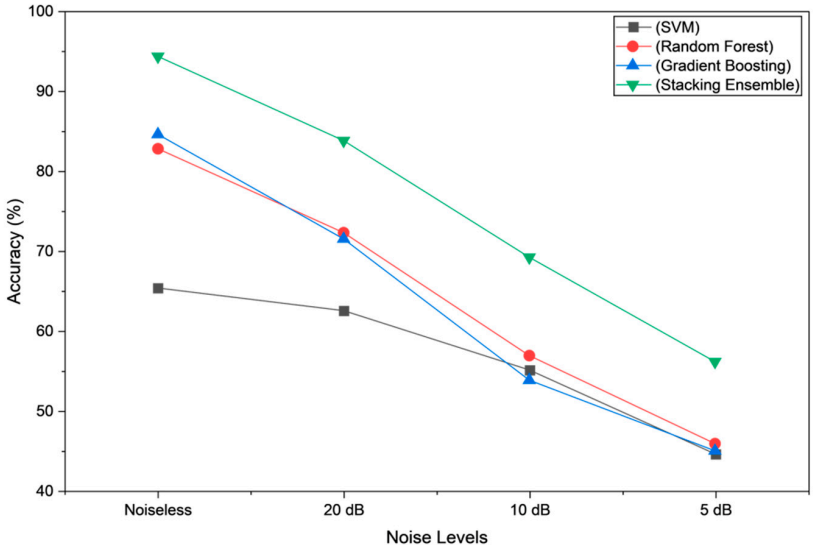


Figure 17. Classification accuracy of 4-op-amp biquad filter under varying noise levels.

6. Conclusions and Discussion

The proposed fault diagnosis framework integrates time-domain transient features, frequency-domain circuit parameters, and VMD-derived IMF statistical features into a unified hierarchical feature vector. Although VMD has been widely applied in mechanical engineering, its application to analog electronic circuits remains limited. This work provides a novel assessment of noise impact on IMF-based diagnostic systems using mean squared error (MSE) evaluated at the individual IMF level. The results consistently show that IMF1 demonstrates the highest robustness to noise across both circuit topologies, suggesting that lower-frequency intrinsic modes retain more discriminative fault information under degraded SNR conditions. This finding has practical implications for feature prioritization in noise-prone diagnostic systems.

The stacking ensemble comprising Random Forest, Gradient Boosting, and Extra Trees as base learners, with Logistic Regression as the meta-learner, effectively addresses topological ambiguity in analog circuits, where different components within the same topology can produce similar responses. This was particularly evident in the biquad circuit, where faults associated with resistors R8 and R9 were poorly classified by individual models due to their structurally similar circuit responses. The ensemble approach demonstrated superior classification performance across both topologies with a zero-false-alarm rate under fault-free conditions, confirming the reliability of the proposed framework. Despite these improvements, residual confusion between structurally similar components persists, indicating that intrinsic response similarity limits perfect separability when faults produce nearly indistinguishable system dynamics rather than reflecting limitations of the learning models themselves.

However, several limitations must be acknowledged. The framework primarily considers single parametric faults with relatively large deviations of $\pm 50\%$, representing a controlled environment rather than fully realistic operating conditions. Smaller parametric variations and simultaneous multi-component fault conditions, which commonly occur in practical electronic systems, are not considered in this study. Furthermore, the analysis is performed entirely on simulated datasets under controlled noise injection, and hardware non-idealities such as temperature variation, parasitic effects, measurement uncertainty, and electromagnetic interference are not explicitly modeled, which may influence performance in real-world implementations.

This work presents a noise-aware multi-domain stacking ensemble framework for analog circuit fault diagnosis validated on two benchmark topologies, namely the Sallen–Key bandpass filter and the fourth-order biquad high-pass filter. The primary contribution lies in the construction of a hierarchical feature vector that fuses time-domain, frequency-domain, and VMD-derived statistical features, enabling robust fault classification across varying noise levels. The proposed stacking ensemble consistently outperforms individual classifiers across all tested SNR conditions, demonstrating both accuracy and reliability. A key finding of this work is that IMF1 consistently exhibits the highest noise robustness and can serve as a basis for feature prioritization in IMF-based diagnostic systems. The framework achieves strong classification performance with a zero-false-alarm rate under fault-free conditions, confirming its practical reliability. Future work will focus on the application of deep learning techniques for scalogram-based analysis and experimental validation of the proposed approach on physical hardware under real electromagnetic interference conditions, along with extension to simultaneous multi-component fault scenarios.

https://doi.org/10.3390/jsan15040054

Author Contributions: Conceptualization, A.D. and B.M.; methodology, A.D., B.M. and V.A.U.; software, A.D., V.A.U., N.S. and S.B.; validation, A.D. and B.M.; formal analysis, A.D., B.M. and V.A.U.; investigation, A.D., V.A.U., N.S. and S.B.; data curation, A.D.; writing—original draft preparation, A.D. and B.M.; writing—review and editing, B.M.; visualization, A.D., V.A.U., N.S. and S.B.; supervision, B.M.; project administration, B.M.; funding acquisition, B.M. All authors have read and agreed to the published version of the manuscript.

Funding: This research was funded by the University of Idaho Faculty Startup Grant, College of Engineering (Index No. 831707). The authors gratefully acknowledge the financial support provided by the University of Idaho. The authors also acknowledge PSG Institute of Technology and Applied Research, Coimbatore, India, for providing technical support, research facilities, and institutional support that contributed to the successful completion of this work.

Data Availability Statement: The original contributions presented in this study are included in the article. Further inquiries can be directed to the corresponding authors.

Conflicts of Interest: The authors declare no conflict of interest.

References

1. Binu, D.; Kariyappa, B. A survey on fault diagnosis of analog circuits: Taxonomy and state of the art. *AEU-Int. J. Electron. Commun.* **2017**, *73*, 68–83. [CrossRef]
2. Tsoulos, I.G.; Stavrou, V.; Mastorakis, N.E.; Tsalikakis, D. Genconstraint: A programming tool for constraint optimization problems. *SoftwareX* **2019**, *10*, 100355. [CrossRef]
3. Dieste Velasco, M. Soft fault diagnosis in analog electronic circuits using supervised machine learning. *Integration* **2025**, *104*, 102482. [CrossRef]
4. Dieste-Velasco, M. Identification of simultaneous soft faults in analog circuits using a hybrid PSO-machine learning approach. *Circuits Syst. Signal Process.* **2026**, 1–31. [CrossRef]
5. Aminian, M.; Aminian, F. Neural-network based analog-circuit fault diagnosis using wavelet transform as preprocessor. *IEEE Trans. Circuits Syst. II Analog Digit. Signal Process.* **2002**, *47*, 151–156. [CrossRef]
6. Zhao, S.; Liang, X.; Wang, L.; Zhang, H.; Li, G.; Chen, J. A fault diagnosis method for analog circuits based on EEMD-PSO-SVM. *Heliyon* **2024**, *10*, e38064. [CrossRef] [PubMed]
7. Tsoulos, I.G.; Kosmas, O.T.; Stavrou, V. Diracsolver: A tool for solving the Dirac equation. *Comput. Phys. Commun.* **2019**, *236*, 237–243. [CrossRef]
8. Lu, X.; Yang, C.; Wu, Q.; Wang, J.; Lu, Z.; Sun, S.; Liu, K.; Shao, D. Research on analog circuit soft fault diagnosis method based on mathematical morphology fractal dimension. *Electronics* **2022**, *12*, 184. [CrossRef]
9. Ma, S.; Shi, S.; Wan, L.; Zhang, Y.; Zhang, G. A fault diagnosis method for analog circuits based on VMD-CFOA-ELM. *Preprint* **2025**. [CrossRef] [PubMed]
10. Yuan, X.; Yang, S.; Wang, W.; Sheng, Y.; Zhuang, X.; Yin, J. A fault diagnosis method for analog circuits based on improved TQWT and inception model. *Symmetry* **2024**, *16*, 720. [CrossRef]
11. Gao, T.; Yang, J.; Jiang, S. A novel fault diagnosis method for analog circuits with noise immunity and generalization ability. *Neural Comput. Appl.* **2021**, *33*, 10537–10550. [CrossRef]
12. Arabi, A.; Ayad, M.; Bourouba, N.; Benziane, M.; Griche, I.; Ghoneim, S.S.; Ali, E.; Elsisi, M.; Ghaly, R.N. An efficient method for faults diagnosis in analog circuits based on machine learning classifiers. *Alex. Eng. J.* **2023**, *77*, 109–125. [CrossRef]
13. Prusty, S.; Patnaik, S.; Dash, S.K. Skcv: Stratified k-fold cross-validation on ML classifiers for predicting cervical cancer. *Front. Nanotechnol.* **2022**, *4*, 972421. [CrossRef]
14. Dragomiretskiy, K.; Zosso, D. Variational mode decomposition. *IEEE Trans. Signal Process.* **2013**, *62*, 531–544. [CrossRef]
15. Lu, X.; Zou, Y.; Wu, Q.; Yang, L.; Zhu, Y. Analog circuit fault diagnosis model based on WOA and improved SDAE. *IEICE Electron. Express* **2025**, *22*, 20240633. [CrossRef]
16. Friedman, J.H. Greedy function approximation: A gradient boosting machine. *Ann. Stat.* **2001**, *29*, 1189–1232. [CrossRef]
17. Patri, A.; Patnaik, Y. Random forest and stochastic gradient tree boosting based approach for the prediction of airfoil self-noise. *Procedia Comput. Sci.* **2015**, *46*, 109–121. [CrossRef]
18. Singhal, M.; Ahmad, G. Fault diagnosis in analog circuits using stacking ensemble machine learning approach. *Circuits Syst. Signal Process.* **2025**, *44*, 6255–6275. [CrossRef]
19. Alhams, A.; Abdelhadi, A.; Badri, Y.; Sassi, S.; Renno, J. Enhanced bearing fault diagnosis through trees ensemble method and feature importance analysis. *J. Vib. Eng. Technol.* **2024**, *12*, 109–125. [CrossRef]

20. Catelani, M.; Fort, A. Soft fault detection and isolation in analog circuits: Some results and a comparison between a fuzzy approach and radial basis function networks. *IEEE Trans. Instrum. Meas.* **2002**, *51*, 196–202. [CrossRef]
21. Chicco, D.; Warrens, M.J.; Jurman, G. The coefficient of determination r-squared is more informative than SMAPE, MAE, MAPE, MSE and RMSE in regression anal YSIS evaluation. *Peerj Comput. Sci.* **2021**, *7*, 623. [CrossRef] [PubMed]
22. Zhang, S.; Shan, S.; Shen, Y.; Li, C.; Zhang, K.; Wei, H. Causal feature-aware dynamic graph neural network for open-set domain generalization diagnosis in multi-sensor systems. *Adv. Eng. Inform.* **2026**, *70*, 104227. [CrossRef]

Disclaimer/Publisher's Note: The statements, opinions and data contained in all publications are solely those of the individual author(s) and contributor(s) and not of MDPI and/or the editor(s). MDPI and/or the editor(s) disclaim responsibility for any injury to people or property resulting from any ideas, methods, instructions or products referred to in the content.